

# DenoMamba: A fused state-space model for low-dose CT denoising

Şaban Öztürk\*, Oğuz Can Duran, and Tolga Çukur

**Abstract**—Low-dose computed tomography (LDCT) lower potential risks linked to radiation exposure while relying on advanced denoising algorithms to maintain diagnostic quality in reconstructed images. The reigning paradigm in LDCT denoising is based on neural network models that learn data-driven image priors to separate noise evoked by dose reduction from underlying tissue signals. Naturally, the fidelity of these priors depend on the model’s ability to capture the broad range of contextual features evident in CT images. Earlier convolutional neural networks (CNN) are highly adept at efficiently capturing short-range spatial context, but their limited receptive fields reduce sensitivity to interactions over longer distances. Although transformers based on self-attention mechanisms have recently been posed to increase sensitivity to long-range context, they can suffer from suboptimal performance and efficiency due to elevated model complexity, particularly for high-resolution CT images. For high-quality restoration of LDCT images, here we introduce DenoMamba, a novel denoising method based on state-space modeling (SSM), that efficiently captures short- and long-range context in medical images. Following an hourglass architecture with encoder-decoder stages, DenoMamba employs a spatial SSM module to encode spatial context and a novel channel SSM module equipped with a secondary gated convolution network to encode latent features of channel context at each stage. Feature maps from the two modules are then consolidated with low-level input features via a convolution fusion module (CFM). Comprehensive experiments on LDCT datasets with 25% and 10% dose reduction demonstrate that DenoMamba outperforms state-of-the-art denoisers with average improvements of 1.4dB PSNR, 1.1% SSIM, and 1.6% RMSE in recovered image quality.

**Index Terms**—low-dose computed tomography, denoising, restoration, state space, sequence models, Mamba

## I. INTRODUCTION

A cornerstone in modern medical imaging, CT irradiates the body with a beam of X-rays to furnish detailed cross-sectional views of anatomy [1]. Unlike conventional radiography, CT relies on acquisition of multiple snapshots as the X-ray beam is rotated around the body, causing substantially elevated exposure to ionizing radiation with potential risks including cancer [2], [3]. A mainstream approach to alleviate these

health risks involves CT protocols that cap the tube current or exposure time to lower the number of incident photons and thereby the radiation dose [4]. However, as the signal-to-noise ratio (SNR) scales with the number of incident photons, dose reduction inevitably increases the noise component in CT images, significantly degrading image quality and potentially obscuring diagnostic features. Consequently, development of effective denoising methods is imperative to maintaining the diagnostic utility of LDCT images acquired under high dose reduction [5]. The success of a denoising method inherently depends on its ability to separate noise components from tissue signals. Note that tissues in a given cross-sectional view can be broadly distributed across contiguous or segregated clusters [6], so tissue signals exhibit both local and global correlations [7]. Meanwhile, the noise variance in LDCT images scales with the intensity of the tissue signal, so the noise component can also show a degree of local and global correlations [8], [9]. Thus, an effective denoising method should be able to discern unique patterns of contextual features that distinguish the noise component from tissue signals.

In recent years, learning-based methods rooted in deep neural network models have replaced traditional approaches in LCDT denoising [10], [11], given their ability to adapt to the distribution of imaging data [12]–[15]. Earlier studies in this domain have predominantly employed CNN-based models to process noisy LDCT images [16]–[18]. Several architectural improvements have also been posed over basic CNNs to boost performance, including use of residual connections [19] and edge-sharpening convolutions to alleviate spatial smoothing [20], and use of multi-scale networks to enhance capture of short- and long-range context [21], [22]. Commonly, these CNN models employ compact convolutional filters for image processing, enabling them to benefit from linear model complexity with respect to image dimensions, and high expressiveness for local contextual features that are critical in delineating detailed tissue structure [23]–[25]. However, the locality bias of convolutional filters inevitably restricts sensitivity to long-range contextual features in LDCT images [26], [27]. As such, CNNs can suffer from poor denoising performance especially near regions of heterogeneous tissue composition, where understanding contextual relationships is crucial for distinguishing signal from noise.

A recent alternative to CNNs are transformer-based models that employ self-attention operators in place of convolutional filters [9], [28]–[30]. Transformers process images as a sequence of tokens (i.e., image patches), and perform non-local filtering via self-attention for improved sensitivity to long-range contextual features. At the same time, however, such

This study was supported by TUBA GEBIP 2015 and BAGEP 2017 fellowships awarded to T. Çukur (Corresponding author: Şaban Öztürk, [saban.ozturk@hbv.edu.tr](mailto:saban.ozturk@hbv.edu.tr)).

Authors are with the Dept. of Electrical-Electronics Engineering and National Magnetic Resonance Research Center (UMRAM), Bilkent University, Ankara, Turkey, 06800. Ş. Öztürk is also with the Ankara Hacı Bayram Veli University, Ankara, Turkey. T. Çukur is also with the Neuroscience Graduate Program Bilkent University, Ankara, Turkey, 06800.

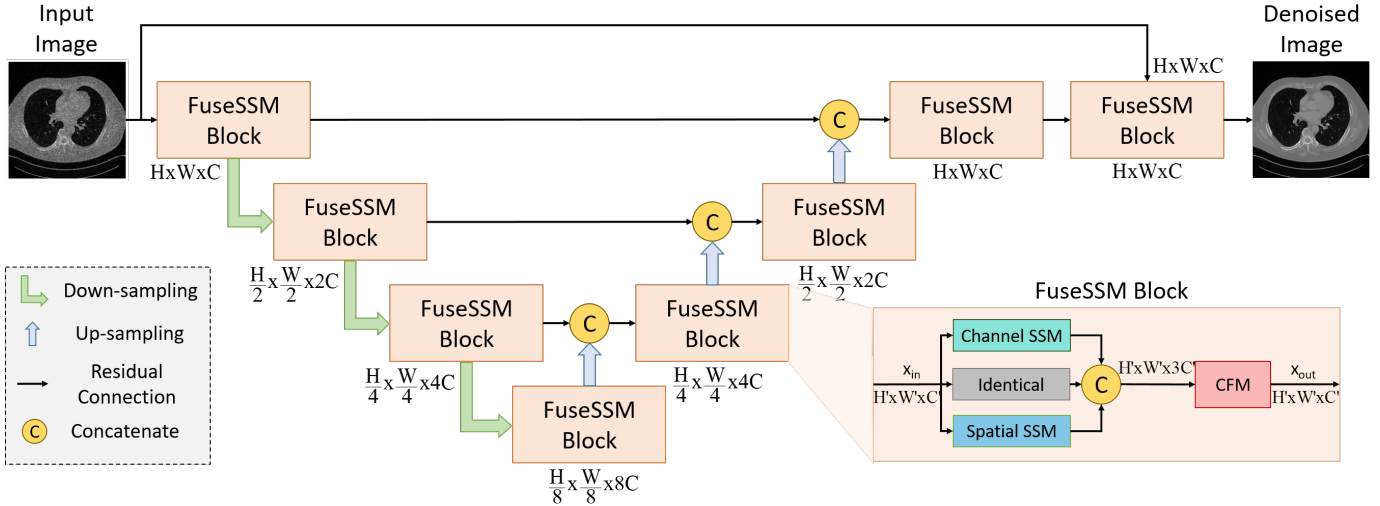


Fig. 1: Overall architecture of DenoMamba. The proposed model comprises encoder-decoder stages that are residually connected with long skip connections to propagate low-level representations. In the encoder stages, input feature maps are projected through cascaded FuseSSM blocks, and spatially downsampled while the channel dimensionality is increased. In the decoder stages, input feature maps are back-projected through cascaded FuseSSM blocks, and spatially upsampled while the channel dimensionality is reduced. The proposed FuseSSM blocks use a spatial SSM module to extract spatial context and a channel SSM module to extract channel context. Afterwards, original input features and their spatial- and channel-wise contextualized representations are fused in a convolutional fusion module (CFM).

non-local filtering induces quadratic model complexity with respect to sequence length [31], [32]. A common approach to mitigate complexity has been to split the image into relatively large-sized patches, which naturally limits spatial precision [31], [33], [34]. A number of strategies have been considered to address this limitation, including architectures with separate branches for low- and high-frequency image components [35], architectures with edge enhancing filters [36], hybrid CNN-transformer architectures [37], and pyramidal transformer architectures with implicit biases from CNN models [9], [38]–[40], and dual-attention architectures have been developed to effectively process various features [30]. Note that despite their relatively improved efficiency, these variant transformer models can still be more complex than CNNs, thus suffering from suboptimal learning on modest-sized training datasets. An emerging framework to capture long-range context under linear complexity employs state-space models (SSM) [41], [42]. Recent medical imaging studies have reported promising results based on a selective SSM variant (Mamba) in downstream tasks such as segmentation and classification [43]–[45]. Yet, the potential of SSMs for image denoising in LDCT remains unexplored.

Here we introduce a novel SSM-based model, DenoMamba, to achieve improved performance in LDCT image denoising without elevating model complexity. DenoMamba leverages an hourglass architecture with encoder-decoder stages constructed with novel FuseSSM blocks (Fig. 1). Each FuseSSM block convolutionally fuses the spatial context captured by a spatial SSM module with the channel context captured by a novel channel SSM module. The proposed channel SSM module employs a secondary gated convolution network following the SSM layer in order to extract latent hidden features of channel context. Meanwhile, to improve preservation of low-level representations in LDCT images, the SSM modules are

equipped with residual connections and hierarchical features extracted by encoder stages are projected onto decoder stages via long-range residual connections. These building blocks empower DenoMamba to capture both short- and long-range contextual information in LDCT images, with comparable model complexity to conventional CNNs. Comprehensive evaluations on LDCT datasets acquired with 25% and 10% of nominal radiation doses demonstrate the superior performance of DenoMamba compared to state-of-the-art baselines. Code to implement DenoMamba is publicly available at <https://github.com/icon-lab/DenoMamba>.

## Contributions

- To our knowledge, DenoMamba is the first LDCT denoising method in the literature that leverages state-space modeling to capture spatial and channel context.
- DenoMamba employs a novel architecture based on convolutional fusion of spatial and channel SSM modules, enabling it to consolidate a comprehensive set of contextual features.
- A novel channel SSM module is introduced that extracts low- and high-level latent features of channel context by cascading a transposed SSM layer with a subsequent gated convolution network.
- DenoMamba is demonstrated to offer superior image quality to state-of-the-art convolutional and transformer models for LDCT denoising across various levels of dose reduction.

## II. RELATED WORK

### A. Learning-based Models in LDCT Denoising

Many earlier methods in the domain of LDCT denoising have adopted CNN models that process images via compact,

shift-invariant convolutional filters [46], [47]. The implicit locality bias of convolutional filters enables CNNs to attain computational efficiency, learn effectively from modest size datasets, and offer high sensitivity to short-range contextual features in medical images [48]. Yet, vanilla CNNs also manifest a number of key limitations; and a number of architectural improvements have been sought over the years to address them [49]. To improve learning and denoising performance, residual connections have been included in an autoencoder architecture [19]. To improve preservation of detailed tissue structure in denoised images, models that separately process low- and high-frequency image components [16], [17], [21], models embodying Sobel convolutional layers to emphasize tissue boundaries [20], and multi-scale models that fuse features extracted at different scales have been proposed [22], [50]. To lower model complexity without compromising performance, autoencoder architectures based on quadratic neurons have been proposed [18]. To improve realism in denoised CT images, generative adversarial models [51], and denoising diffusion probabilistic models [] have been considered. To enhance denoising performance near rare pathology, multiplicative attention layers have been embedded in CNN models [52]. While these advancements have helped push the performance envelope in LDCT denoising, CNN models often struggle to capture long-range contextual features in medical images due to the locality bias of convolutional filters.

As an alternative to CNNs, recent studies have introduced transformer models that instead process images via non-local, shift-variant self-attention filters [53]. Driven by the similarities between all possible pairs of image tokens regardless of their spatial distance, self-attention filters enable transformers to offer exceptional sensitivity to not only short-range but also long-range contextual features [31], [54]. Yet, the quadratic complexity of self-attention with respect to image size has limited the spatial precision at which transformers can be utilized. A group of studies have proposed hybrid CNN-transformer backbones [28], [55], dilated transformers [35], and windowed transformers [40] that alleviate model complexity by lowering feature maps dimensions that are provided to the transformer modules. However, these previous models inevitably diminish the sensitivity benefits of transformers for long-range contextual features towards relatively high spatial resolutions. Aiming to alleviate such losses in spatial precision, models that separately process low- and high-frequency image components [35], [56], models that use Sobel convolutional filters or gradient maps [30], [36], models that employ edge enhancement [37], and segmented models [1], [32] have been proposed. That said, it remains a significant challenge in transformer-based method to maintain sensitivity to long-range context in high-resolution LDCT images, without introducing prohibitive computational burden.

### B. SSM Models in Medical Imaging

SSMs are an emerging framework in machine learning, offering the ability to capture long-range context without the significant computational demands of transformers [57]–[61]. Building on this framework, several recent medical imaging

---

### Algorithm 1: Overall Network Mapping

---

**Input:**  $x$ : Noisy input image of dimensions  $H \times W$   
**Output:**  $\hat{y}$ : Denoised output image of dimensions  $H \times W$

Initialize model parameters  $\theta = \{\theta_{\text{enc}}^{1:K}, \theta_{\text{dec}}^{K:1}\}$ .  
 Set  $x_{\text{enc}}^0 = x$ .  
**for**  $k = 1$  **to**  $K$  **do**  
     **if**  $k \neq K$  **then**  
          $x_{\text{enc}}^k = \text{Down}(\text{FuseSSM}_{\text{enc}}^k(x_{\text{enc}}^{k-1}; \theta_{\text{enc}}^k))$ ,  
         where  $\text{Down}(\cdot)$  resamples to  $H/2^k \times W/2^k \times 2^k C$ .  
     **else**  
          $x_{\text{enc}}^k = \text{FuseSSM}_{\text{enc}}^k(x_{\text{enc}}^{k-1}; \theta_{\text{enc}}^k)$ .  
 Set  $x_{\text{dec}}^K = x_{\text{enc}}^K$ .  
**for**  $k = K$  **to**  $1$  **do**  
     **if**  $k \neq 1$  **then**  
          $x_{\text{dec}}^{k-1} = \text{FuseSSM}_{\text{dec}}^k(\text{Up}(x_{\text{dec}}^k) + x_{\text{enc}}^{k-1}; \theta_{\text{dec}}^k)$ ,  
         where  $\text{Up}(\cdot)$  resamples to  
          $H/2^{k-2} \times W/2^{k-2} \times 2^{k-2} C$ .  
     **else**  
          $x_{\text{dec}}^{k-1} = \text{FuseSSM}_{\text{dec}}^k(x_{\text{dec}}^k + x_{\text{enc}}^{k-1}; \theta_{\text{dec}}^k)$ .  
**return**  $\hat{y} = x_{\text{dec}}^1$

---

studies have devised SSM-based models for challenging tasks such as segmentation [43], [62], classification [45], synthesis [27], reconstruction [63], and landmark detection [64] with promising results. Yet, to our knowledge, the potential of SSMs in medical image denoising has not been previously explored. Here, we introduce DenoMamba as the very first SSM-based model for LDCT denoising in the literature. Our proposed model employs a novel architecture comprising FuseSSM blocks, which extract contextual features in the channel dimension via a channel SSM module, contextual features in the spatial dimension via a spatial SSM module, and merges these contextual features with low-level representations in input feature maps via a convolutional fusion module. As such, DenoMamba comprehensively models contextual features in LDCT images and maintains high spatial precision without the burdening computational overhead of transformer-based methods.

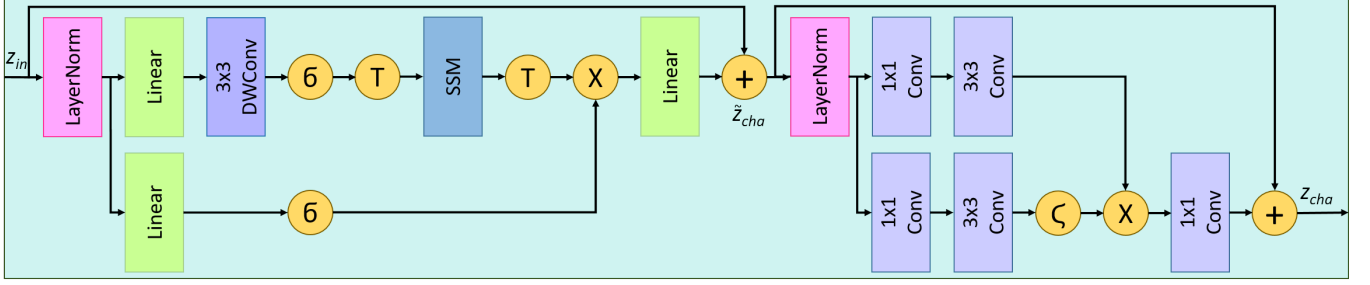
## III. THEORY

### A. Problem Definition

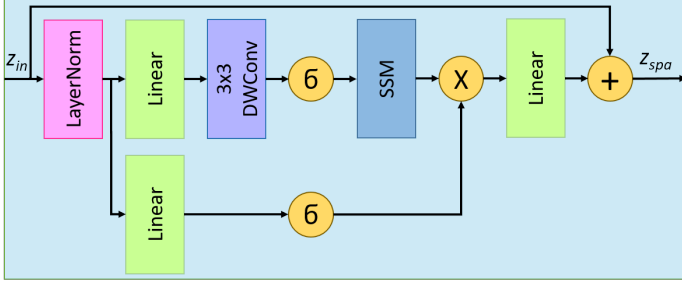
LCDT image denoising involves suppression of elevated Poisson noise in low-dose scans due to reduced number of incident photons from the X-ray beam. In learning-based methods, this is attempted with a neural network model that is trained to map noisy LDCT images onto denoised images that would be consistent with a normal dose CT (NDCT) scan. Let  $x \in \mathbb{R}^{H \times W}$  denote the noisy LDCT image, and  $y \in \mathbb{R}^{H \times W}$  denote the corresponding NDCT image, where  $H$ ,  $W$  are the image height and width, respectively. Given a training set of  $N$  image pairs  $(x_{tr}[i], y_{tr}[i])$  with  $i \in [1 N]$ , the network model  $f_{\theta}(\cdot)$  with parameters  $\theta$  can be trained as follows:

$$\theta^* = \underset{\theta}{\text{argmin}} \sum_{i=1}^N \|f_{\theta}(x_{tr}[i]) - y_{tr}[i]\|_2^2, \quad (1)$$

## a) Channel SSM



## b) Spatial SSM



## c) CFM

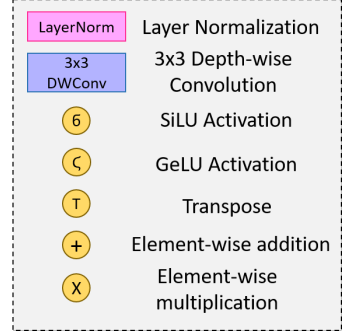
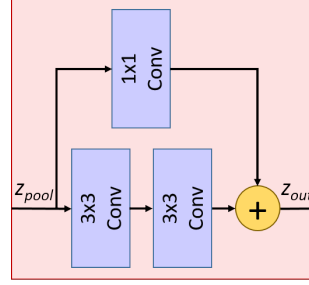


Fig. 2: Inner modules of the FuseSSM blocks. Each FuseSSM block comprises a channel SSM module, a spatial SSM module, and a CFM module. (a) The channel SSM module performs convolutional encoding of image tokens after layer normalization, and processes the transposed feature map via an SSM layer to capture an initial set of contextual features across the channel dimension. To further extract a second set of latent features, this initial set is projected through a gated convolutional network, and the two sets of contextual features are residually combined. (b) The spatial SSM modules performs convolutional encoding of image tokens after layer normalization, and processes the feature map via an SSM layer to capture contextual features across the spatial dimension. (c) The CFM module pools original input features along with contextual features from the channel and spatial SSM modules, and fuses them via convolutional layers.

The optimal parameters  $\theta^*$  are those that minimize the loss function, thereby yielding a model capable of effectively attenuating noise in LDCT images. Upon successful training, this model can be deployed to process novel LDCT images, generating high-fidelity denoised outputs as  $\hat{y}_{test}[i] = f_{\theta^*}(x_{test}[i])$ .

## B. DenoMamba

DenoMamba is the first LDCT image denoising method in the literature that uses SSMs to model spatial and channel context, to our knowledge. It employs a novel architecture based on FuseSSM blocks, which serve to capture a comprehensive set of contextual features across spatial and channel dimensions, while maintaining favorable balance in model complexity. In the following subsections, we describe the overall model architecture and the inner structure of FuseSSM blocks in detail.

1) *Overall Model Architecture*: As depicted in Fig. 1, DenoMamba follows an hourglass structure with  $K$  encoder and  $K$  decoder stages. Each stage is implemented as a cascade of multiple FuseSSM blocks. Starting from the noisy LDCT image  $x$  taken as model input, encoder stages serve to extract latent contextualized representations via FuseSSM blocks and resample the feature map dimensions. Let  $x_{enc}^k$  denotes the feature map at the output of the  $k$ th encoder stage, with  $k \in [1, 2, \dots, K]$  and  $x_{enc}^0 = x$ . The mapping through the  $k$ th

encoder stage can be described as follows:

$$x_{enc}^k = \begin{cases} \text{Down}(\text{FuseSSM}_{enc}^k(x_{enc}^{k-1}; \theta_{enc}^k)), & \text{if } k \neq K \\ \text{FuseSSM}_{enc}^k(x_{enc}^{k-1}; \theta_{enc}^k), & \text{if } k = K \end{cases} \quad (2)$$

where  $\theta_{enc}^k$  denotes the parameters of FuseSSM blocks in the  $k$ th encoder stage,  $\text{Down}(\cdot)$  denotes a learnable downsampling operator, and  $x_{enc}^k \in \mathbb{R}^{\frac{H}{2^k} \times \frac{W}{2^k} \times 2^k C}$ . Note that downsampling is performed at the end of all encoder stages, except for the final stage (i.e.,  $k = K$ ).

Starting from the encoded feature map  $x_{enc}^K$ , decoder stages then serve to reconstruct a denoised image  $\hat{y}$  from the latent representations via FuseSSM blocks and resampling of feature map dimensions. The decoder stages follow a mirror-reversed order, such that  $x_{dec}^k$  denotes the feature map at the output of the  $k$ th decoder stage, with  $k \in [K, K-1, \dots, 1]$  and  $x_{dec}^K = x_{enc}^K$ . Thus, the mapping through the  $k$ th decoder stage can be described as follows:

$$x_{dec}^{k-1} = \begin{cases} \text{FuseSSM}_{dec}^k(\text{Up}(x_{dec}^k) + x_{enc}^{k-1}; \theta_{dec}^k), & \text{if } k \neq 1 \\ \text{FuseSSM}_{dec}^k(x_{dec}^k + x_{enc}^{k-1}; \theta_{dec}^k), & \text{if } k = 1 \end{cases} \quad (3)$$

where  $\theta_{dec}^k$  denotes the parameters of FuseSSM blocks in the  $k$ th decoder stage,  $\text{Up}(\cdot)$  denotes a learnable upsampling operator, and  $x_{dec}^{k-1} \in \mathbb{R}^{\frac{H}{2^{k-2}} \times \frac{W}{2^{k-2}} \times 2^{k-2} C}$ . Note that upsampling is performed on the decoder feature map  $x_{dec}^k$  in the beginning of all decoder stages, except for the final stage (i.e.,  $k = 1$ ). Furthermore, encoder feature maps from the respective encoder stage  $x_{enc}^{k-1}$  are residually added onto

the input decoder maps to improve preservation of low-level structural representations in LDCT images. The final output of DenoMamba is taken as  $\hat{y} = x_{\text{dec}}^1$ . The forward mappings through DenoMamba that project the noisy LDCT image onto the denoised image estimate are outlined in Alg. 1.

2) **FuseSSM blocks**: DenoMamba is constructed with novel FuseSSM blocks that comprise a spatial SSM module to capture contextual representations in the spatial domain and a channel SSM module to capture contextual representations in the channel domain [42]. We uniquely propose to project input feature maps to the FuseSSM module across three parallel pathways that propagate the contextualized representations from spatial and channel SSM modules, along with original input features. Afterwards, these representations are merged via a convolutional fusion module (CFM). For a given FuseSSM block, a schematic of the individual components are depicted in Fig. 2, and corresponding network mappings through the components are outlined in Alg. 2.

The design of FuseSSM blocks in encoder and decoder stages are near identical, apart from variability in feature map dimensions. Thus, here we will describe the projections through a FuseSSM block at a given stage without distinguishing between encoder/decoder segments. Assuming that the input feature map at the  $k$ th stage is  $x_{\text{in}} = x^k \in \mathbb{R}^{H' \times W' \times C'}$ , the respective FuseSSM block first splits the input across the spatial dimensions into  $P = \frac{H'W'}{p^2}$  non-overlapping patches of size  $(p, p)$  to form a respective sequence  $z_{\text{in}}$  [65]. This input sequence is then projected through three parallel pathways to compute contextualized representations:

$$\{z_{\text{cha}}, z_{\text{in}}, z_{\text{spa}}\} = \{\text{SSM}_{\text{cha}}(z_{\text{in}}), \text{I}(z_{\text{in}}), \text{SSM}_{\text{spa}}(z_{\text{in}})\}, \quad (4)$$

where  $\text{SSM}_{\text{cha}}$  denotes the channel SSM,  $\text{SSM}_{\text{spa}}$  denotes the spatial SSM, and  $\text{I}$  denotes identity transformation. Finally, the extracted contextual representations are pooled and convolutionally fused in the CFM module:

$$z_{\text{pool}} = \text{Concat}(z_{\text{cha}}, z_{\text{in}}, z_{\text{spa}}), \quad (5)$$

$$z_{\text{out}} = \text{Conv}^{1 \times 1}(z_{\text{pool}}) \oplus \text{Conv}^{3 \times 3}(\text{Conv}^{3 \times 3}(z_{\text{pool}})), \quad (6)$$

where  $\text{Concat}$  denotes a concatenation operator that pools feature maps across the channel dimension,  $\text{Conv}^{1 \times 1}$  and  $\text{Conv}^{3 \times 3}$  respectively denote  $1 \times 1$  and  $3 \times 3$  convolutional layers, and  $\oplus$  is the element-wise addition operator. The output sequence  $z_{\text{out}}$  is remapped onto the image domain as  $x_{\text{out}}$ , taken as the output of the FuseSSM block.

**Spatial SSM**: Within the spatial SSM module, a first branch linearly embeds the input sequence and uses a nonlinearity to produce a gating variable  $GP$ :

$$GP_{\text{spa}} = \sigma(f_{\text{lin}}(z_{\text{in}})), \quad (7)$$

where  $\sigma$  is an activation function and  $f_{\text{lin}}$  denotes a learnable linear mapping. A second branch performs linear embedding and convolutional encoding, followed by state-space modeling:

$$M_{\text{spa}} = \text{SSM}(\sigma(\text{DWConv}^{3 \times 3}(f_{\text{lin}}(z_{\text{in}})))), \quad (8)$$

where  $\text{SSM}$  denotes a state-space layer,  $\text{DWConv}^{3 \times 3}$  refers to depth-wise convolution of kernel size  $3 \times 3$ .

Here, the state-space layer is implemented based on the Mamba variant in [42], which performs selective scanning across two spatial dimensions for sequence expansion, per-

---

**Algorithm 2: Mapping through a FuseSSM block**


---

**Input:**  $x_{\text{in}}$ : Input feature map of dim.  $H' \times W' \times C'$   
**Output:**  $x_{\text{out}}$ : Output feature map of dim.  $H' \times W' \times C'$

▷ Split  $x_{\text{in}}$  into  $p \times p$  patches to form sequence  $z_{\text{in}}$

**Module 1: Spatial SSM**

$$M_{\text{spa}} = \text{SSM}(\sigma(\text{DWConv}^{3 \times 3}(f_{\text{lin}}(z_{\text{in}}))))$$

$$GP = \sigma(f_{\text{lin}}(z_{\text{in}}))$$

$$z_{\text{spa}} = z_{\text{in}} + f_{\text{lin}}(GP \odot M_{\text{spa}})$$

**Module 2: Channel SSM**

$$M_{\text{cha}} = f_T(\text{SSM}(f_T(\sigma(\text{DWConv}^{3 \times 3}(f_{\text{lin}}(z_{\text{in}}))))))$$

$$GP = \sigma(f_{\text{lin}}(z_{\text{in}})) \quad \triangleright \text{gating}$$

$$\tilde{z}_{\text{cha}} = z_{\text{in}} + f_{\text{lin}}(GP \odot M_{\text{cha}})$$

$$GP^2 = \zeta(\text{DWConv}^{3 \times 3}(\text{Conv}^{1 \times 1}(\tilde{z}_{\text{cha}})))$$

$$z_{\text{cha}} =$$

$$\text{Conv}^{1 \times 1}(GP^2 \odot \text{DWConv}^{3 \times 3}(\text{Conv}^{1 \times 1}(\tilde{z}_{\text{cha}}))) + \tilde{z}_{\text{cha}}$$

**Module 3: CFM**

$$z_{\text{pool}} = \text{Concat}(z_{\text{cha}}, z_{\text{in}}, z_{\text{spa}})$$

$$z_{\text{out}} = \text{Conv}^{1 \times 1}(z_{\text{pool}}) \oplus \text{Conv}^{3 \times 3}(\text{Conv}^{3 \times 3}(z_{\text{pool}}))$$

▷ Remap  $z_{\text{out}}$  onto the image domain to form  $x_{\text{out}}$

**return**  $x_{\text{out}}$

---

forms state-space modeling, and recombines the output. The resultant state-space model can be characterized as:

$$h[n] = \mathbf{A}h[n-1] + \mathbf{B}z[n], \quad (9)$$

$$\bar{z}[n] = \mathbf{C}h[n] + \mathbf{D}z[n], \quad (10)$$

where  $h$  is the hidden state,  $z$  is the input sequence,  $\bar{z}$  is the output sequence,  $n$  is the sequence index, and  $\mathbf{A} \in \mathbb{R}^{N, N}$ ,  $\mathbf{B} \in \mathbb{R}^{N, 1}$ ,  $\mathbf{C} \in \mathbb{R}^{1, N}$ ,  $\mathbf{D} \in \mathbb{R}$  are learnable parameters, with  $N$  indicating the state dimensionality.

To compute the module output,  $M_{\text{spa}}$  is gated with  $GP$ , and the result is linearly projected and combined with the input sequence through a residual connection:

$$z_{\text{spa}} = z_{\text{in}} + (f_{\text{lin}}(GP_{\text{spa}} \odot M_{\text{spa}})), \quad (11)$$

where  $\odot$  denotes the Hadamard product operator.

**Channel SSM**: Similar to the spatial SSM module, within the channel SSM module, a first branch produces a gating variable and a second branch performs state-space modeling on the input sequence to capture contextual interactions in the channel dimension:

$$GP_{\text{cha}} = \sigma(f_{\text{lin}}(z_{\text{in}})), \quad (12)$$

$$M_{\text{cha}} = \text{SSM}((\sigma(\text{DWConv}^{3 \times 3}(f_{\text{lin}}(z_{\text{in}}))))^{\top})^{\top}, \quad (13)$$

where  $\top$  denotes the transpose operator. Differing from the spatial SSM module, the channel SSM module model channel context by transposing the input sequence prior to and after the projection through the state-space layer. This results in an intermediate set of contextual representations derived as:

$$\tilde{z}_{\text{cha}} = z_{\text{in}} + (f_{\text{lin}}(GP_{\text{cha}} \odot M_{\text{cha}})). \quad (14)$$

Note that many layers in DenoMamba can perform spatial encoding, such as the depth-wise convolutional layers in FuseSSM blocks and downsampling/upsampling layers across encoder/decoder stages. Collectively, these layers can learn a hierarchy of latent features of spatial context. Yet, channel encoding is primarily performed in the state-space layers of the channel SSM module, limiting the information captured on

channel context. To address this limitation, here we propose a novel channel SSM module that incorporates a gated convolution network to extract latent features of channel context. For this purpose, a gating variable is first computed:

$$GP^2 = \zeta(\text{DWConv}^{3 \times 3}(\text{Conv}^{1 \times 1}(\tilde{z}_{\text{cha}}))). \quad (15)$$

This variable is then used to modulate latent features of  $\tilde{z}_{\text{cha}}$ :

$$z_{\text{cha}} = \text{Conv}^{1 \times 1}(GP^2 \odot \text{DWConv}^{3 \times 3}(\text{Conv}^{1 \times 1}(\tilde{z}_{\text{cha}}))) + \tilde{z}_{\text{cha}}. \quad (16)$$

**3) Learning Procedures:** Given a training set of image pairs  $(x_{tr}[i], y_{tr}[i])$  with  $i \in [1, N]$ , DenoMamba with parameters  $\theta_{\text{enc}}, \theta_{\text{dec}}$  is trained via a mean-squared error loss term:

$$\{\theta_{\text{enc}}^*, \theta_{\text{dec}}^*\} = \underset{\theta_{\text{enc}}, \theta_{\text{dec}}}{\text{argmin}} \sum_{i=1}^N \left\| \text{FuseSSM}_{\text{dec}}^{(K:1)} \left( \text{FuseSSM}_{\text{enc}}^{(1:K)}(x_{tr}[i]; \theta_{\text{enc}}^{(1:K)}); \theta_{\text{dec}}^{(K:1)} \right) - y_{tr}[i] \right\|_2^2. \quad (17)$$

Using the trained parameters  $\{\theta_{\text{enc}}^*, \theta_{\text{dec}}^*\}$ , the model can be deployed to process a novel LDCT image from the test set  $x_{test}[i]$  to estimate a denoised output  $\hat{y}_{test}[i]$  as:

$$\hat{y}_{test}[i] = \text{FuseSSM}_{\text{dec}}^{(K:1)} \left( \text{FuseSSM}_{\text{enc}}^{(1:K)} \left( x_{test}[i]; \theta_{\text{enc}}^{*(1:K)} \right); \theta_{\text{dec}}^{*(K:1)} \right) \quad (18)$$

## IV. EXPERIMENTAL SETUP

### A. Datasets

Demonstrations of denoising performance were conducted on datasets derived from the 2016 NID-AAPM Mayo Clinic Low Dose CT Grand Challenge, comprising contrast-enhanced abdominal CT scans obtained 70 s after administration of iodinated contrast agents [66]. Separate datasets were considered based on two different dose reduction levels, resulting in 25% and 10% radiation dose with respect to nominal values. Normal dose CT (NDCT) scans were acquired at 120 kV reference tube potential with 200 effective mAs as quality reference radiation dose. Meanwhile, LDCT at 25% radiation dose assumed 50 effective mAs, and LDCT at 10% radiation dose assumed 20 effective mAs [66]. Dose reduction in LDCT scans was attained by adding Poisson noise onto NDCT images [8], [31].

For both 25%-dose and 10%-dose datasets, the training and validation sets were formed by reconstructing CT images at 1-mm slice thickness. A total of 760 cross-sectional NDCT-LDCT image pairs from 9 subjects were included in the training set, and 35 image pairs from 1 subject were included in the validation set. Meanwhile, the test set was formed by reconstructing four different sets of CT images based on two distinct kernels (Siemens B30 and D45), and two distinct slice thicknesses (1 mm and 3 mm), resulting in multiple parameter combinations: B30-1mm, D45-1mm, B30-3mm, and D45-3mm. A total of 200 image pairs from 20 subjects were included in the test set. All images were resized to  $256 \times 256$  in-plane resolution, and there was no subject overlap among the training, validation and test sets.

**TABLE I:** Performance of DenoMamba variants built by varying the number of encoder-decoder stages  $K$ , by varying the number of initial feature channels at the first stage  $C$ , and by varying the number of cascaded FuseSSM blocks in the final stage  $R$ . PSNR (dB), SSIM (%) and RMSE (%) metrics are listed on the validation set for the 25%-dose dataset, along with the number of model parameters in millions.

		Param. (M)	↑ PSNR (dB)	↑ SSIM (%)	↓ RMSE (%)
$K$	3	47.75	42.30	96.73	8.41
	4	112.62	42.41	96.75	8.31
	5	441.99	42.28	96.73	8.47
$C$	32	51.10	42.18	98.24	8.55
	48	112.62	42.41	96.75	8.31
	56	154.47	42.26	96.73	8.45
$R$	2	112.62	42.41	96.75	8.31
	4	113.77	42.33	96.74	8.37
	6	114.92	42.32	96.72	8.36

**TABLE II:** Performance of DenoMamba variants built by ablating the channel SSM module (w/o cha. SSM), by ablating the spatial SSM module (w/o spa. SSM), by ablating the CFM module (w/o CFM), by ablating the gated convolution network to extract latent features in the channel SSM module (w/o GCN), and by ablating identity mapping pathway that pools input features in the CFM module (w/o Iden.). PSNR, SSIM, RMSE and the number of model parameters are listed for the 25%-dose dataset.

	Param. (M)	↑ PSNR (dB)	↑ SSIM (%)	↓ RMSE (%)
w/o cha. SSM	95.49	41.93	96.69	8.76
w/o spa. SSM	95.49	42.10	96.71	8.62
w/o CFM	112.62	42.27	96.73	8.41
w/o GCN	112.62	42.32	96.75	8.38
w/o Iden.	95.49	42.05	96.46	8.70
<b>DenoMamba</b>	112.62	42.41	96.75	8.31

### B. Competing Methods

We demonstrated DenoMamba against several state-of-the-art methods for LDCT denoising. Competing methods included CNN models (RED-CNN, N2N, EDCNN), transformer models (UFormer, LIT-Former), generative adversarial models (WGAN, DU-GAN), an auto-encoder model (QAE) and a diffusion model (IDDPMP).

*DenoMamba:* A  $K = 4$  stage encoder-decoder architecture was used, where the number of FuseSSM blocks cascaded varied as [4, 6, 6, 8] across encoder stages and as [6, 6, 4, 2] across decoder stages, respectively. Spatial resolution was lowered by a factor of 2 following each encoder stage except for the final one, while the channel dimensionality was set as [48, 96, 192, 384] across stages. Conversely, spatial resolution was increased by a factor of 2 after each decoder stage except for the final one, with the channel dimensionality set as [192, 96, 48, 48] across stages. Both channel and spatial SSM modules used a state expansion factor of 16, a local convolution width of 4, and a block expansion factor of 2.

*RED-CNN:* A CNN model was considered that combines convolution layers, deconvolution layers, and shortcut con-

**TABLE III:** Denoising performance of competing methods on the 25%-dose LDCT dataset. Results are given separately for test sets comprising 1-mm slices, 3-mm slices, and all slices. PSNR (dB), SSIM (%) and RMSE (%) metrics are listed as mean±std across the test set. Boldface marks the method that offers the best performance for each metric.

	1-mm slices			3-mm slices			Overall		
	↑ PSNR (dB)	↑ SSIM (%)	↓ RMSE (%)	↑ PSNR (dB)	↑ SSIM (%)	↓ RMSE (%)	↑ PSNR (dB)	↑ SSIM (%)	↓ RMSE (%)
RED-CNN	40.48 ± 3.16	95.82 ± 2.28	10.14 ± 0.38	43.91 ± 2.90	97.99 ± 1.01	6.78 ± 0.25	42.19 ± 3.03	96.91 ± 1.65	8.46 ± 0.32
N2N	40.25 ± 3.08	95.81 ± 2.31	10.31 ± 0.37	43.62 ± 2.87	97.97 ± 1.03	6.98 ± 0.27	41.94 ± 2.98	96.90 ± 1.67	8.65 ± 0.32
EDCNN	40.31 ± 3.22	95.63 ± 2.33	10.34 ± 0.39	43.89 ± 2.90	97.93 ± 1.11	6.79 ± 0.25	42.10 ± 3.06	96.78 ± 1.72	8.57 ± 0.32
UFormer	39.87 ± 2.85	95.63 ± 2.25	10.71 ± 0.38	42.23 ± 2.73	97.88 ± 1.03	8.15 ± 0.28	41.05 ± 2.79	96.76 ± 1.64	9.43 ± 0.33
LIT-Former	39.33 ± 2.94	94.84 ± 2.61	11.42 ± 0.39	42.54 ± 2.69	97.25 ± 1.13	7.82 ± 0.26	40.93 ± 2.82	96.05 ± 1.87	9.62 ± 0.33
WGAN	38.12 ± 2.91	93.04 ± 3.08	12.71 ± 0.45	41.47 ± 2.17	96.56 ± 1.49	8.46 ± 0.24	39.79 ± 2.54	94.80 ± 2.29	10.59 ± 0.35
DU-GAN	38.27 ± 3.36	92.36 ± 4.46	13.18 ± 0.51	41.75 ± 2.85	96.60 ± 1.79	8.67 ± 0.31	40.01 ± 3.11	94.48 ± 3.13	10.92 ± 0.41
QAE	39.52 ± 2.84	94.68 ± 2.57	11.29 ± 0.40	42.68 ± 2.51	97.14 ± 1.30	7.66 ± 0.24	41.10 ± 2.68	95.91 ± 1.94	9.47 ± 0.32
IDDPM	39.71 ± 2.38	95.52 ± 2.23	10.79 ± 0.33	42.37 ± 2.06	97.58 ± 1.09	8.02 ± 0.24	41.04 ± 2.22	96.55 ± 1.66	9.40 ± 0.29
<b>DenoMamba</b>	<b>40.91 ± 3.01</b>	<b>96.03 ± 2.38</b>	<b>9.63 ± 0.38</b>	<b>44.48 ± 2.69</b>	<b>98.11 ± 1.10</b>	<b>6.39 ± 0.28</b>	<b>42.69 ± 2.85</b>	<b>97.07 ± 1.74</b>	<b>8.00 ± 0.33</b>

nections [19]. Convolutional and deconvolutional kernels were initialized with a Gaussian distribution of zero mean and 0.01 standard deviation.

*N2N*: A CNN model was considered that uses self-supervised learning on noisy images generated via random neighbor subsampling and a regularizer for noise suppression [67]. The hyperparameter  $\gamma$ , which controls the strength of the regularizer, was set to 2.

*EDCNN*: A CNN model was considered that employs a trainable Sobel convolution kernel for edge detection and dense connections [20]. The hyperparameter  $\omega_p$  in the compound loss function was set to 0.01.

*UFormer*: A transformer model was considered that uses a hierarchical encoder-decoder architecture and local window-based self-attention [68]. The number of attention heads was taken as  $\{1, 2, 8, 8\}$  across encoder stages.

*LIT-Former*: A transformer model was considered that uses transformer modules for in-plane and through-plane dimensions [1]. The number of attention heads was taken as  $\{1, 2, 4, 8\}$  across encoder stages.

*WGAN*: A generative adversarial model that uses a Wasserstein distance loss function was considered [51]. Loss term weights were set as  $\lambda = 10$ ,  $\lambda_1 = 0.1$ ,  $\lambda_2 = 0.1$ .

*DU-GAN*: A generative adversarial model that operates in both image and gradient domains was considered [69]. Loss terms weights were set as  $\lambda_{adv} = 0.1$ ,  $\lambda_{img} = 1$ , and  $\lambda_{grad} = 20$ .

*QAE*: An autoencoder model was considered that implements an encoder-decoder architecture based on quadratic neurons for efficiency [18]. Quadratic convolutional layers used a kernel size of 3 and a stride of 1.

*IDDPM*: A conditional diffusion model was considered that generated NDCT images starting from Gaussian noise images, with additional guidance from the LCDT image provided as input [70]. The number of diffusion steps was taken as 1000.

### C. Modeling Procedures

Models were implemented using the PyTorch framework and trained on a system equipped with an NVidia RTX 3090

GPU and 128GB of RAM. Training was performed via the Adam optimizer with parameters  $\beta_1 = 0.5$  and  $\beta_2 = 0.999$  [71]. For all competing methods, the learning rate was set to  $1 \times 10^{-4}$ , and the number of epochs was set to 100. The initial learning rate was halved after every 30 epochs to promote gradual model refinement. During training, all images were resized to  $256 \times 256$  pixels. Data were split into training, validation and test sets with no subject-level overlap between the three sets. Key model hyperparameters were selected via cross-validation for each competing method. Model performance was then evaluated on the test set with Peak Signal-to-Noise Ratio (PSNR), Structural Similarity Index (SSIM), and Root Mean Square Error (RMSE) metrics. Results for 1-mm and 3-mm slice thicknesses were separately reported, along with pooled results across both thicknesses. Results were pooled across B30 and D45 reconstruction kernels as they did not show notable differences. Note that higher values of PSNR and SSIM, and lower values of RMSE indicate improved model performance. Significance of performance differences between competing methods were evaluated via non-parametric Wilcoxon signed-rank tests ( $p < 0.05$ ).

## V. RESULTS

### A. Ablation Studies

We conducted a systematic set of ablation studies to examine the importance of key design parameters and building elements in DenoMamba. First, we assessed the influence of the number of encoder-decoder stages  $K$ , the number of initial feature channels at the first encoder stage  $C$ , and the number of FuseSSM blocks cascaded at the last decoder stage  $R$ . Variant models were built by varying the values of  $K$ ,  $C$ , and  $R$  while remaining parameters were kept fixed. Table I lists performance metrics of DenoMamba variants on the 25%-dose dataset, along with the number of model parameters. We find that variants for  $K = 4$ ,  $C = 48$ , and  $R = 2$  yield near-optimal performance, validating the proposed selection of design parameters.

We then assessed the influence of critical building elements in DenoMamba on denoising performance. Several ablated

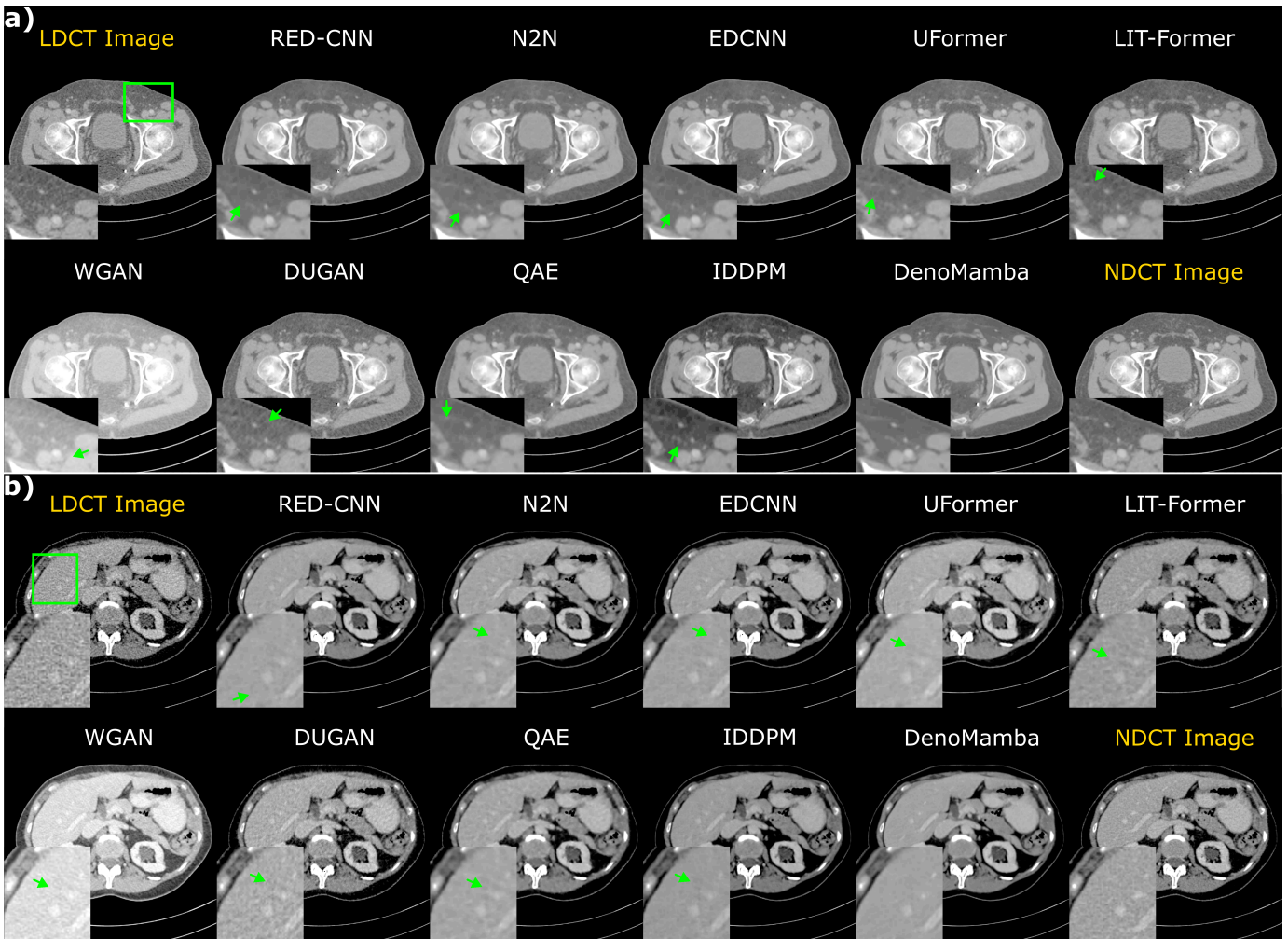


**Fig. 3:** Denoising results from the 25%-dose LDCT dataset are depicted as **a** and **b** for two representative cross-sections. Images recovered by competing methods are shown along with the noisy LDCT image (i.e., model input), and the NDCT image (i.e., ground truth). Zoom-in displays and arrows are used to showcase regions with visible differences in image quality among competing methods. Compared to baselines, DenoMamba produces denoised CT images with lower noise and artifact levels and more accurate delineation of detailed tissue structure, closely aligned with the ground truth.

variants were formed for this purpose. A ‘w/o cha. SSM’ variant was formed by ablating the channel SSM module from FuseSSM blocks. A ‘w/o spa. SSM’ variant was formed by ablating the spatial SSM module from FuseSSM blocks. A ‘w/o CFM’ variant was formed by replacing the channel fusion module in FuseSSM blocks with a simple element-wise addition operator to combine contextual features from spatial/channel SSM modules with original input features. A ‘w/o GCN’ variant was formed by ablating the gated convolutional network in channel SSM modules that extracts latent contextual features across the channel dimension. A ‘w/o Iden.’ variant was formed by ablating the identity transformation pathway in the CFM module that propagates original input features to the convolutional fusion layer. Table II lists performance metrics for DenoMamba and ablated variants on the 25%-dose dataset, along with the number of model parameters. We find that DenoMamba outperforms all ablated variants ( $p < 0.05$ ), indicating the important of these individual building elements for LDCT denoising performance.

## B. Comparison Studies

Next, we demonstrated DenoMamba via comparisons against several state-of-the-art methods from the LDCT denoising literature. Specifically, competing methods included CNN models (RED-CNN, N2N, EDCNN), transformer models (Uformer, LIT-Former), GAN models (WGAN, DU-GAN), an autoencoder model (QAE), and a diffusion model (IDDPM). Experiments were first conducted on the 25%-dose dataset to recover high-quality images from LDCT measurements. Table III lists performance metrics for competing methods separately for a test set comprising 1-mm thick slices, a test set comprising 3-mm thick slices, and an aggregated test set comprising both slice thicknesses. In each individual setting for the test set, we find that DenoMamba significantly outperforms all competing methods ( $p < 0.05$ ). On average, DenoMamba achieves performance improvements of 0.6dB PSNR, 0.2% SSIM, 0.6% RMSE over CNNs; 1.7dB PSNR, 0.7% SSIM, 1.5% RMSE over transformers; 2.8dB PSNR, 2.4% SSIM, 2.8% RMSE over GANs; 1.6dB PSNR, 1.2%



**TABLE IV:** Denoising performance of competing methods on the 10%-dose LDCT dataset. Results are given separately for test sets comprising 1-mm slices, 3-mm slices, and all slices. PSNR (dB), SSIM (%) and RMSE (%) metrics are listed as mean $\pm$ std across the test set. Boldface marks the method that offers the best performance for each metric.

	1-mm slices			3-mm slices			Overall		
	$\uparrow$ PSNR (dB)	$\uparrow$ SSIM (%)	$\downarrow$ RMSE (%)	$\uparrow$ PSNR (dB)	$\uparrow$ SSIM (%)	$\downarrow$ RMSE (%)	$\uparrow$ PSNR (dB)	$\uparrow$ SSIM (%)	$\downarrow$ RMSE (%)
RED-CNN	38.17 $\pm$ 2.38	94.82 $\pm$ 2.26	12.89 $\pm$ 0.39	39.60 $\pm$ 2.39	96.89 $\pm$ 1.03	10.94 $\pm$ 0.32	38.88 $\pm$ 2.39	95.85 $\pm$ 1.65	11.91 $\pm$ 0.35
N2N	38.22 $\pm$ 2.35	94.75 $\pm$ 2.35	12.68 $\pm$ 0.36	39.71 $\pm$ 2.47	96.78 $\pm$ 1.14	10.76 $\pm$ 0.33	38.96 $\pm$ 2.41	95.76 $\pm$ 1.74	11.72 $\pm$ 0.35
EDCNN	38.01 $\pm$ 2.56	94.45 $\pm$ 2.43	13.16 $\pm$ 0.41	39.52 $\pm$ 2.42	96.74 $\pm$ 1.13	11.06 $\pm$ 0.33	38.77 $\pm$ 2.49	95.59 $\pm$ 1.78	12.11 $\pm$ 0.37
UFormer	38.12 $\pm$ 2.57	94.87 $\pm$ 2.22	12.91 $\pm$ 0.42	39.42 $\pm$ 2.66	96.78 $\pm$ 1.02	11.24 $\pm$ 0.39	38.77 $\pm$ 2.62	95.82 $\pm$ 1.62	12.08 $\pm$ 0.41
LIT-Former	36.80 $\pm$ 2.06	92.00 $\pm$ 1.90	14.78 $\pm$ 0.38	37.86 $\pm$ 1.87	92.94 $\pm$ 1.09	12.99 $\pm$ 0.29	37.33 $\pm$ 1.97	92.47 $\pm$ 1.50	13.89 $\pm$ 0.34
WGAN	36.58 $\pm$ 2.29	92.91 $\pm$ 2.92	14.98 $\pm$ 0.42	38.15 $\pm$ 2.08	95.52 $\pm$ 1.02	12.43 $\pm$ 0.33	37.37 $\pm$ 2.19	94.22 $\pm$ 1.97	13.70 $\pm$ 0.38
DU-GAN	37.05 $\pm$ 2.51	93.15 $\pm$ 4.01	14.80 $\pm$ 0.51	38.13 $\pm$ 2.41	95.34 $\pm$ 1.75	13.02 $\pm$ 0.43	37.57 $\pm$ 2.46	94.24 $\pm$ 2.88	13.91 $\pm$ 0.47
QAE	37.73 $\pm$ 2.48	94.23 $\pm$ 2.53	13.60 $\pm$ 0.43	39.21 $\pm$ 2.29	96.45 $\pm$ 1.17	11.44 $\pm$ 0.38	38.47 $\pm$ 2.39	95.34 $\pm$ 1.85	12.52 $\pm$ 0.41
IDDPM	37.68 $\pm$ 2.34	93.81 $\pm$ 2.18	13.35 $\pm$ 0.38	38.63 $\pm$ 2.86	95.95 $\pm$ 1.27	12.23 $\pm$ 0.44	38.16 $\pm$ 2.60	94.88 $\pm$ 1.73	12.79 $\pm$ 0.41
<b>DenoMamba</b>	<b>39.05 <math>\pm</math> 2.38</b>	<b>95.27 <math>\pm</math> 2.35</b>	<b>11.63 <math>\pm</math> 0.40</b>	<b>40.39 <math>\pm</math> 2.48</b>	<b>97.22 <math>\pm</math> 1.11</b>	<b>10.10 <math>\pm</math> 0.35</b>	<b>39.72 <math>\pm</math> 2.43</b>	<b>96.24 <math>\pm</math> 1.73</b>	<b>10.86 <math>\pm</math> 0.38</b>

SSIM, 1.5% RMSE over the autoencoder; 1.7dB PSNR, 0.5% SSIM, 1.4% RMSE over the diffusion model. Representative denoised images recovered by competing methods are displayed in Fig. 3. Among baselines, CNN models are generally effective in suppressing local noise patterns within homogeneous tissue regions, albeit they are suboptimal in alleviating noise patterns that extend over longer distances, occasionally inducing perturbations in tissue contrast deviating from ground truth NDCT images. Contrarily, transformers with their enhanced sensitivity to long-range context are better at preserving contrast across heterogeneous tissue regions, but they suffer from residual local noise patterns that manifest as signal intensity fluctuations in homogeneous tissue regions. Although GAN models maintain the highest visual sharpness, this comes at the expense of high levels of residual noise in recovered images. Meanwhile, the autoencoder model shows a degree of spatial blurring, and the diffusion model suffers from inaccuracies in tissue contrast and suboptimal noise suppression. In comparison to baselines, DenoMamba recovers high-quality CT images with reliable suppression of local and global noise patterns, and accurate depiction of tissue structure and contrast.

We also conducted experiments on the 10%-dose dataset to assess competing methods at a relatively more challenging denoising task. Table IV lists performance metrics for competing methods separately for a test set comprising 1-mm thick slices, a test set comprising 3-mm thick slices, and an aggregated test set comprising both slice thicknesses. Corroborating the findings on the 25%-dose dataset, we find that DenoMamba significantly outperforms all competing methods consistently across all examined settings ( $p < 0.05$ ). On average, DenoMamba achieves performance improvements of 0.9dB PSNR, 0.5% SSIM, 1.1% RMSE over CNNs; 1.7dB PSNR, 2.1% SSIM, 2.1% RMSE over transformers; 2.3dB PSNR, 2.0% SSIM, 2.9% RMSE over GANs; 1.3dB PSNR, 0.9% SSIM, 1.7% RMSE over the autoencoder; 1.6dB PSNR, 1.4% SSIM, 1.9% RMSE over the diffusion model. Representative denoised images recovered by competing methods are displayed in Fig. 4. Note that, at the higher 10% dose reduction level, additive Poisson noise becomes more prominent, yielding spatially-

correlated perturbations in LDCT images comparable to native variations in tissue signals. Since distinguishing noise-driven perturbations from actual variations in tissue signals become more challenging, the difficulty of the LDCT denoising task is elevated. We observe that both CNNs and transformers start to suffer from residual noise patterns in locally homogeneous tissue regions, lowering structural accuracy particularly in the vicinity of tissue boundaries. As GAN models intend to maintain high-spatial frequency information in recovered images, they suffer from high levels of residual noise patterns. The autoencoder model shows visible residual noise. While the diffusion models yields generally higher image quality in comparison to other baselines, it suffers from a degree of structural inaccuracy in depiction of detailed tissue structures. Contrarily, DenoMamba offers high-fidelity depiction of detailed tissue structure in CT images with visibly improved noise suppression.

## VI. DISCUSSION

In this study, we introduced a novel denoising method to recover high-quality NDCT images from noisy LDCT images. Previous CNN models offer computational efficiency and higher local precision, albeit they are relatively insensitive to long-range relationships between distant anatomical regions in medical images [48]. While transformer models can address this limitations by leveraging the long-range contextual sensitivity of the self-attention mechanism, they inherently suffer from quadratic model complexity with respect to sequence length, which common approaches to alleviate this complexity result in inevitable losses in spatial precision [72]. Differently from these previous models, DenoMamba employs novel FuseSSM blocks to capture contextual features via state-space modeling across spatial and channel dimensions, while enjoying similar computational efficiency to CNN models. Our demonstrations indicate that DenoMamba achieves superior performance in LDCT denoising against state-of-the-art CNN and transformer methods, with apparent quantitative and qualitative benefits in recovered CT images.

Several technical limitations can be addressed in order to further boost the performance and practicality of DenoMamba.

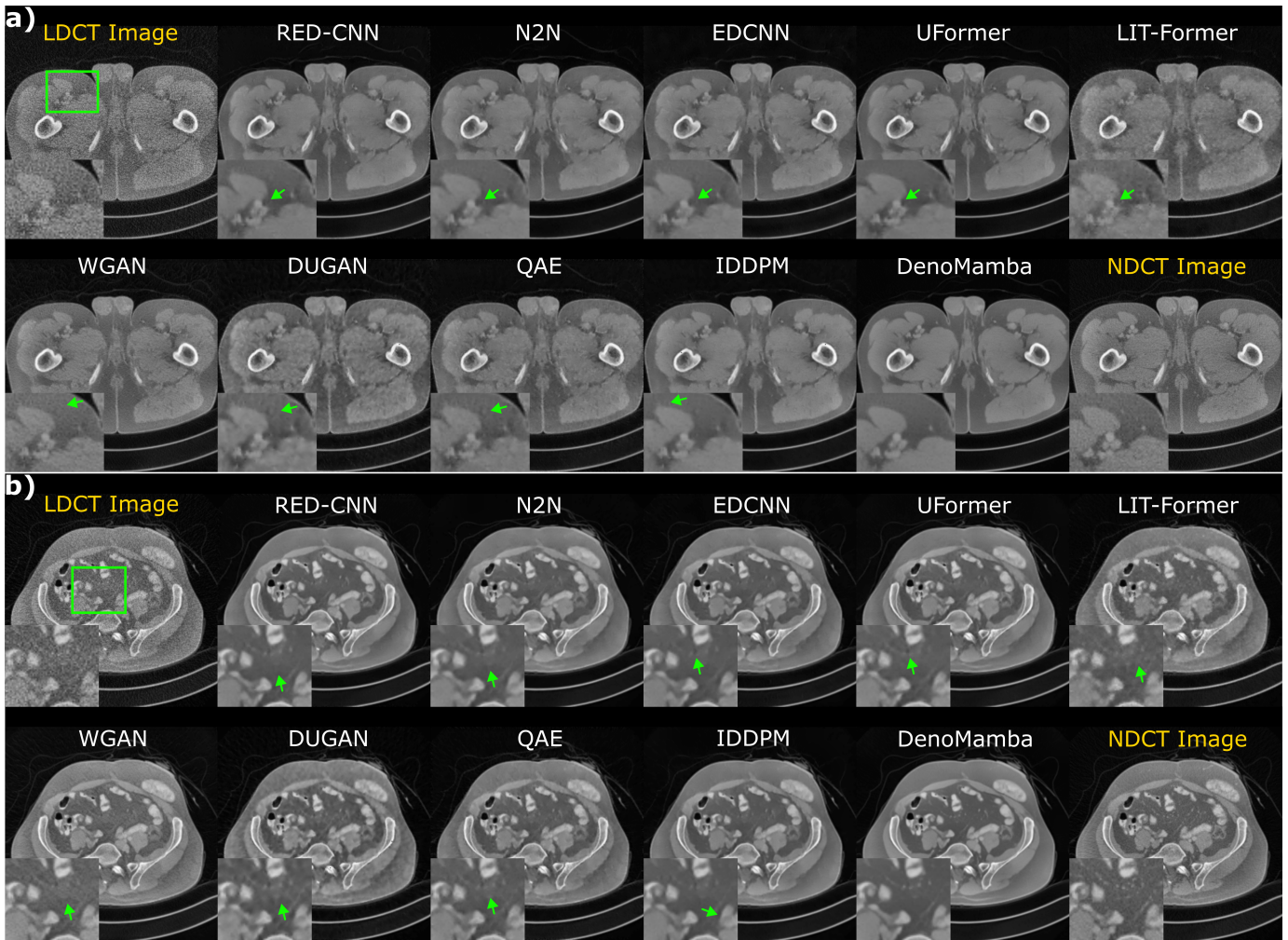


**Fig. 4:** Denoising results from the 10%-dose LDCT dataset are depicted as **a** and **b** for two representative cross-sections. Images recovered by competing methods are shown along with the noisy LDCT image (i.e., model input), and the NDCT image (i.e., ground truth). Zoom-in displays and arrows are used to showcase regions with visible differences in image quality among competing methods. Compared to baselines, DenoMamba produces denoised CT images with lower noise and artifact levels and more accurate delineation of detailed tissue structure, closely aligned with the ground truth.

A first line concerns the nature of denoising tasks used for model training. Here, a separate model was trained for LDCT denoising at each reduction level for radiation dose to maintain high performance. Note that this may lower practicality if highly variable reduction levels are expected to be administered in practice. In those cases, DenoMamba can be trained on LDCT images at varying reduction levels, and model specialization to specific radiation doses could be enhanced by adaptive normalization approaches on feature maps [73]–[75]. This could improve practicality by building a unified model that can be deployed at various dose reduction levels.

A second line of improvements concerns the datasets on which DenoMamba is trained to perform LDCT denoising. Here, we performed supervised learning relying on the availability of paired LDCT-NDCT images from the same set of subjects [76]. Note that, in practice, the curation of such paired datasets can be challenging as it would require repeated CT scans on a given subject at separate radiation doses. In cases where the amount of paired training data that can be collected is limited, a large training set can be curated

by instead adopting cycle-consistent learning procedures on unpaired sets of LDCT and NDCT images [77], [78], or self-supervised learning procedures to train models directly on LDCT measurements [54], [67]. Alternatively, models can be pre-trained for denoising in a domain with abundant data (e.g., natural images), and then transferred to the LDCT domain via fine-tuning [79].

A third line of improvements concerns the loss terms employed to train DenoMamba. Here, we utilized a simple pixel-wise loss term based on mean-squared error, since we observed that this pixel-wise loss offered effective learning of LDCT denoising models on the examined datasets. That said, it might be possible to attain further improvements in recovered image quality by using more sophisticated loss terms including adversarial, score-based or cross-entropy losses [80]–[84]. Particularly within the context of score-based methods that involve iterative sampling procedures, the long-range contextual sensitivity of DenoMamba might offer benefits over conventional score-based models based on CNN backbones. Further work is warranted for a systematic evaluation of

the utility of various loss functions on the performance and reliability of DenoMamba.

## VII. CONCLUSION

Here we introduced a fused state-space model (SSM) for recovery of high-quality images from noisy LDCT measurements. The proposed DenoMamba model leverages an hour-glass architecture implemented with novel FuseSSM blocks. Each FuseSSM block extracts contextual features across spatial and channel dimensions via spatial and channel SSM modules, respectively, and performs fusion of contextual and original input features via a CFM module. This design enables DenoMamba to leverage contextual relationships in LDCT images without elevating computational burden, and to offer superior performance against state-of-the-art LDCT denoising methods. Therefore, DenoMamba holds great promise for performant and efficient LDCT image denoising.

## REFERENCES

- [1] Z. Chen, C. Niu, Q. Gao, G. Wang, and H. Shan, "Lit-former: Linking in-plane and through-plane transformers for simultaneous ct image denoising and deblurring," *IEEE Transactions on Medical Imaging*, vol. 43, no. 5, pp. 1880–1894, 2024.
- [2] S. Li, Y. Liu, R. Yan, H. Zhang, S. Wang, T. Ding, and Z. Gui, "Dd-dcsr: Image denoising for low-dose ct via dual-dictionary deep convolutional sparse representation," *IEEE Transactions on Computational Imaging*, vol. 10, pp. 899–914, 2024.
- [3] Y. Lu, Z. Xu, M. H. Choi, J. Kim, and S.-W. Jung, "Cross-domain denoising for low-dose multi-frame spiral computed tomography," *IEEE Transactions on Medical Imaging*, pp. 1–1, 2024.
- [4] Y. Lei, Y. Tian, H. Shan, J. Zhang, G. Wang, and M. K. Kalra, "Shape and margin-aware lung nodule classification in low-dose ct images via soft activation mapping," *Medical Image Analysis*, vol. 60, p. 101628, 2020.
- [5] S.-Y. Jeon, W. Kim, and J.-H. Choi, "Mm-net: Multiframe and multimask-based unsupervised deep denoising for low-dose computed tomography," *IEEE Transactions on Radiation and Plasma Medical Sciences*, vol. 7, no. 3, pp. 296–306, 2023.
- [6] A. Adam, A. Dixon, J. Gillard, C. Schaefer-Prokop, R. Grainger, and D. Allison, *Grainger & Allison's Diagnostic Radiology*. Elsevier, 2014.
- [7] D. Ellison, S. Love, L. Chimelli, B. Harding, J. Lowe, H. Vinters, S. Brandner, and W. Yong, *Neuropathology: A Reference Text of CNS Pathology*. Elsevier, 2012.
- [8] M. Meng, Y. Wang, M. Zhu, X. Tao, Z. Mao, J. Liao, Z. Bian, D. Zeng, and J. Ma, "Ddt-net: Dose-agnostic dual-task transfer network for simultaneous low-dose ct denoising and simulation," *IEEE Journal of Biomedical and Health Informatics*, vol. 28, no. 6, pp. 3613–3625, 2024.
- [9] D. Wang, F. Fan, Z. Wu, R. Liu, F. Wang, and H. Yu, "Ctformer: convolution-free token2token dilated vision transformer for low-dose ct denoising," *Physics in Medicine and Biology*, vol. 68, no. 6, p. 065012, mar 2023.
- [10] A. Manduca, L. Yu, J. Trzasko, N. Khaylova, J. Koffler, C. McCollough, and J. Fletcher, "Projection space denoising with bilateral filtering and ct noise modeling for dose reduction in ct," *Medical physics*, vol. 36, no. 11, pp. 4911–4919, 2009.
- [11] S. Gu, L. Zhang, W. Zuo, and X. Feng, "Weighted nuclear norm minimization with application to image denoising," in *2014 IEEE Conference on Computer Vision and Pattern Recognition*, 2014, pp. 2862–2869.
- [12] J. Zhang, Z. Shangguan, W. Gong, and Y. Cheng, "A novel denoising method for low-dose ct images based on transformer and cnn," *Computers in Biology and Medicine*, vol. 163, p. 107162, 2023.
- [13] J. Zhang, W. Gong, L. Ye, F. Wang, Z. Shangguan, and Y. Cheng, "A review of deep learning methods for denoising of medical low-dose ct images," *Computers in Biology and Medicine*, vol. 171, p. 108112, 2024.
- [14] N. Saidulu, P. R. Muduli, and A. Dasgupta, "Rhlnet: Robust hybrid loss-based network for low-dose ct image denoising," *IEEE Transactions on Instrumentation and Measurement*, pp. 1–1, 2024.
- [15] J. Huang, K. Chen, Y. Ren, J. Sun, X. Pu, and C. Zhu, "Cross-domain low-dose ct image denoising with semantic preservation and noise alignment," *IEEE Transactions on Multimedia*, pp. 1–11, 2024.
- [16] E. Kang, J. Min, and J. C. Ye, "A deep convolutional neural network using directional wavelets for low-dose x-ray ct reconstruction," *Medical Physics*, vol. 44, no. 10, pp. e360–e375, 2017.
- [17] E. Kang, J. Min, and J. C. Ye, "Wavelet Domain Residual Network (WavResNet) for Low-Dose X-ray CT Reconstruction," *arXiv e-prints*, p. arXiv:1703.01383, Mar. 2017.
- [18] F. Fan, H. Shan, M. K. Kalra, R. Singh, G. Qian, M. Getzin, Y. Teng, J. Hahn, and G. Wang, "Quadratic autoencoder (q-ae) for low-dose ct denoising," *IEEE Transactions on Medical Imaging*, vol. 39, no. 6, pp. 2035–2050, 2020.
- [19] H. Chen, Y. Zhang, M. K. Kalra, F. Lin, Y. Chen, P. Liao, J. Zhou, and G. Wang, "Low-dose ct with a residual encoder-decoder convolutional neural network," *IEEE Transactions on Medical Imaging*, vol. 36, no. 12, pp. 2524–2535, 2017.
- [20] T. Liang, Y. Jin, Y. Li, and T. Wang, "Edcnn: Edge enhancement-based densely connected network with compound loss for low-dose ct denoising," in *2020 15th IEEE International Conference on Signal Processing (ICSP)*, vol. 1, 2020, pp. 193–198.
- [21] X. Jiang, L. Wang, Z. He, and J. Du, "Learning a frequency separation network with hybrid convolution and adaptive aggregation for low-dose ct denoising," in *2021 IEEE International Conference on Bioinformatics and Biomedicine (BIBM)*, 2021, pp. 919–925.
- [22] Z. Li, Y. Liu, H. Shu, J. Lu, J. Kang, Y. Chen, and Z. Gui, "Multi-scale feature fusion network for low-dose ct denoising," *Journal of Digital Imaging*, vol. 36, no. 4, pp. 1808–1825, 2023.
- [23] H. Shan, A. Padole, F. Homayounieh, U. Kruger, R. D. Khera, C. Nitwarangkul, M. K. Kalra, and G. Wang, "Competitive performance of a modularized deep neural network compared to commercial algorithms for low-dose ct image reconstruction," *Nature Machine Intelligence*, vol. 1, no. 6, pp. 269–276, 2019.
- [24] X. Yin, Q. Zhao, J. Liu, W. Yang, J. Yang, G. Quan, Y. Chen, H. Shu, L. Luo, and J.-L. Coatrieux, "Domain progressive 3d residual convolution network to improve low-dose ct imaging," *IEEE Transactions on Medical Imaging*, vol. 38, no. 12, pp. 2903–2913, 2019.
- [25] Z. Li, Y. Liu, P. Zhang, J. Lu, S. Ren, and Z. Gui, "Adaptive weighted total variation expansion and gaussian curvature guided low-dose ct image denoising network," *Biomedical Signal Processing and Control*, vol. 94, p. 106329, 2024.
- [26] O. Dalmaz, M. Yurt, and T. Çukur, "ResViT: Residual vision transformers for multi-modal medical image synthesis," *IEEE Trans Med Imaging*, vol. 44, no. 10, pp. 2598–2614, 2022.
- [27] O. F. Atli, B. Kabas, F. Arslan, M. Yurt, O. Dalmaz, and T. Çukur, "I2I-Mamba: Multi-modal medical image synthesis via selective state space modeling," *arXiv e-prints*, p. arXiv:2405.14022, May 2024.
- [28] J. Yuan, F. Zhou, Z. Guo, X. Li, and H. Yu, "Hcformer: hybrid cnn-transformer for ldct image denoising," *Journal of Digital Imaging*, vol. 36, no. 5, pp. 2290–2305, 2023.
- [29] H. Li, X. Yang, S. Yang, D. Wang, and G. Jeon, "Transformer with double enhancement for low-dose ct denoising," *IEEE Journal of Biomedical and Health Informatics*, vol. 27, no. 10, pp. 4660–4671, 2023.
- [30] G. Jiang, T. Luo, H. Xu, S. Nie, Y. Song, and Z. He, "Gdaformer: Gradient-guided dual attention transformer for low-dose ct image denoising," *Biomedical Signal Processing and Control*, vol. 94, p. 106260, 2024.
- [31] L. Yang, Z. Li, R. Ge, J. Zhao, H. Si, and D. Zhang, "Low-dose ct denoising via sinogram inner-structure transformer," *IEEE Transactions on Medical Imaging*, vol. 42, no. 4, pp. 910–921, 2023.
- [32] L. Zhu, Y. Han, X. Xi, H. Fu, S. Tan, M. Liu, S. Yang, C. Liu, L. Li, and B. Yan, "Stednet: Swin transformer-based encoder-decoder network for noise reduction in low-dose ct," *Medical Physics*, vol. 50, no. 7, pp. 4443–4458, 2023.
- [33] H. Chen, Y. Wang, T. Guo, C. Xu, Y. Deng, Z. Liu, S. Ma, C. Xu, C. Xu, and W. Gao, "Pre-trained image processing transformer," in *2021 IEEE/CVF Conference on Computer Vision and Pattern Recognition (CVPR)*, 2021, pp. 12 294–12 305.
- [34] J. Liang, J. Cao, G. Sun, K. Zhang, L. Van Gool, and R. Timofte, "Swinir: Image restoration using swin transformer," in *2021 IEEE/CVF International Conference on Computer Vision Workshops (ICCVW)*, 2021, pp. 1833–1844.
- [35] Z. Zhang, L. Yu, X. Liang, W. Zhao, and L. Xing, "TransCT: Dual-path Transformer for Low Dose Computed Tomography," *arXiv e-prints*, p. arXiv:2103.00634, Feb. 2021.
- [36] A. Luthra, H. Sulakhe, T. Mittal, A. Iyer, and S. Yadav, "Eformer: Edge Enhancement based Transformer for Medical Image Denoising," *arXiv e-prints*, p. arXiv:2109.08044, Sep. 2021.
- [37] Q. Yiyu and Q. Zhiwei, "Low-dose ct image reconstruction method based on cnn and transformer coupling network," *CT Theory and Applications*, vol. 31, no. 6, pp. 697–707, 2022.
- [38] D. Wang, Z. Wu, and H. Yu, "Ted-net: Convolution-free t2t vision transformer-based encoder-decoder dilation network for low-dose ct denoising," in *Machine Learning in Medical Imaging: 12th International Workshop, MLMI 2021, Held in Conjunction with MICCAI 2021, Strasbourg, France, September 27, 2021, Proceedings 12*. Springer, 2021, pp. 416–425.

- [39] B. Zhang, Y. Zhang, B. Wang, X. He, F. Zhang, and X. Zhang, "Denoising swin transformer and perceptual peak signal-to-noise ratio for low-dose ct image denoising," *Measurement*, vol. 227, p. 114303, 2024.
- [40] M. Jian, X. Yu, H. Zhang, and C. Yang, "Swinct: feature enhancement based low-dose ct images denoising with swin transformer," *Multimedia Systems*, vol. 30, no. 1, p. 1, 2024.
- [41] L. Zhu, B. Liao, Q. Zhang, X. Wang, W. Liu, and X. Wang, "Vision mamba: Efficient visual representation learning with bidirectional state space model," *arXiv:2401.09417*, 2024.
- [42] Y. Liu, Y. Tian, Y. Zhao, H. Yu, L. Xie, Y. Wang, Q. Ye, and Y. Liu, "Vmamba: Visual state space model," *arXiv:2401.10166*, 2024.
- [43] J. Ma, F. Li, and B. Wang, "U-mamba: Enhancing long-range dependency for biomedical image segmentation," *arXiv:2401.04722*, 2024.
- [44] J. Ruan and S. Xiang, "VM-UNet: Vision Mamba UNet for Medical Image Segmentation," *arXiv:2402.02491*, 2024.
- [45] Y. Yue and Z. Li, "Medmamba: Vision mamba for medical image classification," *arXiv:2403.03849*, 2024.
- [46] J. Wang, T. Li, H. Lu, and Z. Liang, "Penalized weighted least-squares approach to sinogram noise reduction and image reconstruction for low-dose x-ray computed tomography," *IEEE Transactions on Medical Imaging*, vol. 25, no. 10, pp. 1272–1283, 2006.
- [47] M. Balda, J. Hornegger, and B. Heismann, "Ray contribution masks for structure adaptive sinogram filtering," *IEEE Transactions on Medical Imaging*, vol. 31, no. 6, pp. 1228–1239, 2012.
- [48] Y. Korkmaz, S. U. H. Dar, M. Yurt, M. Ozbey, and T. Çukur, "Unsupervised MRI reconstruction via zero-shot learned adversarial transformers," *IEEE Trans Med Imaging*, vol. 41, no. 7, pp. 1747–1763, 2022.
- [49] D. Wu, K. Kim, G. El Fakhri, and Q. Li, "A Cascaded Convolutional Neural Network for X-ray Low-dose CT Image Denoising," *arXiv e-prints*, p. arXiv:1705.04267, May 2017.
- [50] Z. Guo, F. Zhou, Y. Chen, and J. Yuan, "A low-dose ct image denoising method combining multistage network and edge protection," *Tehnički vjesnik*, vol. 29, no. 3, pp. 1059–1067, 2022.
- [51] Q. Yang, P. Yan, Y. Zhang, H. Yu, Y. Shi, X. Mou, M. K. Kalra, Y. Zhang, L. Sun, and G. Wang, "Low-dose ct image denoising using a generative adversarial network with wasserstein distance and perceptual loss," *IEEE Transactions on Medical Imaging*, vol. 37, no. 6, pp. 1348–1357, 2018.
- [52] M. Li, W. Hsu, X. Xie, J. Cong, and W. Gao, "SACNN: Self-attention convolutional neural network for low-dose CT denoising with self-supervised perceptual loss network," *IEEE Trans. Med. Imag.*, vol. 39, no. 7, pp. 2289–2301, 2020.
- [53] Ş. Öztürk, M. Yiğit Turalı, and T. Çukur, "HydraViT: Adaptive Multi-Branch Transformer for Multi-Label Disease Classification from Chest X-ray Images," *arXiv e-prints*, p. arXiv:2310.06143, Oct. 2023.
- [54] Y. Korkmaz, T. Çukur, and V. M. Patel, "Self-supervised mri reconstruction with unrolled diffusion models," in *MICCAI*, 2023, pp. 491–501.
- [55] S.-Y. Zhang, Z.-X. Wang, H.-B. Yang, Y.-L. Chen, Y. Li, Q. Pan, H.-K. Wang, and C.-X. Zhao, "Hformer: highly efficient vision transformer for low-dose ct denoising," *Nuclear Science and Techniques*, vol. 34, no. 4, p. 61, 2023.
- [56] J. Kang, Y. Liu, P. Zhang, N. Guo, L. Wang, Y. Du, and Z. Gui, "Fsformer: A combined frequency separation network and transformer for ldct denoising," *Computers in Biology and Medicine*, vol. 173, p. 108378, 2024.
- [57] R. Deng and T. Gu, "CU-Mamba: Selective State Space Models with Channel Learning for Image Restoration," *arXiv e-prints*, p. arXiv:2404.11778, Apr. 2024.
- [58] M. Shahab Sepehri, Z. Fabian, and M. Soltanolkotabi, "Serpent: Scalable and Efficient Image Restoration via Multi-scale Structured State Space Models," *arXiv e-prints*, p. arXiv:2403.17902, Mar. 2024.
- [59] Y. Shi, B. Xia, X. Jin, X. Wang, T. Zhao, X. Xia, X. Xia, and W. Yang, "VmambaIR: Visual State Space Model for Image Restoration," *arXiv e-prints*, p. arXiv:2403.11423, Mar. 2024.
- [60] G. Fu, F. Xiong, J. Lu, and J. Zhou, "SSUMamba: Spatial-Spectral Selective State Space Model for Hyperspectral Image Denoising," *arXiv e-prints*, p. arXiv:2405.01726, May 2024.
- [61] H. Guo, J. Li, T. Dai, Z. Ouyang, X. Ren, and S.-T. Xia, "MambaIR: A Simple Baseline for Image Restoration with State-Space Model," *arXiv e-prints*, p. arXiv:2402.15648, Feb. 2024.
- [62] Z. Xing, T. Ye, Y. Yang, G. Liu, and L. Zhu, "Segmamba: Long-range sequential modeling mamba for 3d medical image segmentation," *arXiv:2401.13560*, 2024.
- [63] J. Huang, L. Yang, F. Wang, Y. Nan, A. I. Aviles-Rivero, C.-B. Schönlieb, D. Zhang, and G. Yang, "MambaMIR: An Arbitrary-Masked Mamba for Joint Medical Image Reconstruction and Uncertainty Estimation," *arXiv e-prints*, p. arXiv:2402.18451, Feb. 2024.
- [64] H. Gong, L. Kang, Y. Wang, X. Wan, and H. Li, "nnMamba: 3D Biomedical Image Segmentation, Classification and Landmark Detection with State Space Model," *arXiv e-prints*, p. arXiv:2402.03526, Feb. 2024.
- [65] I. Tolstikhin, N. Houlsby, A. Kolesnikov, L. Beyer, X. Zhai, T. Unterthiner, J. Yung, A. Steiner, D. Keysers, J. Uszkoreit *et al.*, "Mlp-mixer: An all-mlp architecture for vision," 2021.
- [66] C. McCollough, "Tu-fg-207a-04: overview of the low dose ct grand challenge," *Medical physics*, vol. 43, no. 6Part35, pp. 3759–3760, 2016.
- [67] T. Huang, S. Li, X. Jia, H. Lu, and J. Liu, "Neighbor2neighbor: Self-supervised denoising from single noisy images," in *2021 IEEE/CVF Conference on Computer Vision and Pattern Recognition (CVPR)*, 2021, pp. 14 776–14 785.
- [68] Z. Wang, X. Cun, J. Bao, W. Zhou, J. Liu, and H. Li, "Uformer: A general u-shaped transformer for image restoration," in *2022 IEEE/CVF Conference on Computer Vision and Pattern Recognition (CVPR)*, 2022, pp. 17 662–17 672.
- [69] Z. Huang, J. Zhang, Y. Zhang, and H. Shan, "Du-gan: Generative adversarial networks with dual-domain u-net-based discriminators for low-dose ct denoising," *IEEE Transactions on Instrumentation and Measurement*, vol. 71, pp. 1–12, 2022.
- [70] A. Q. Nichol and P. Dhariwal, "Improved denoising diffusion probabilistic models," in *International conference on machine learning*. PMLR, 2021, pp. 8162–8171.
- [71] D. P. Kingma and J. Ba, "Adam: A method for stochastic optimization," in *Int. Conf. Learn. Represent.*, 2015.
- [72] N. Kodali, J. Hays, J. Abernethy, and Z. Kira, "On convergence and stability of GANs," *arXiv:1705.07215*, 2017.
- [73] A. Güngör, S. U. Dar, Ş. Öztürk, Y. Korkmaz, G. Elmas, M. Özbey, and T. Çukur, "Adaptive diffusion priors for accelerated MRI reconstruction," *Med Image Anal*, vol. 88, p. 102872, 2023.
- [74] O. Dalmaz, M. U. Mirza, G. Elmas, M. Ozbey, S. U. Dar, E. Ceyani, K. K. Oguz, S. Avestimehr, and T. Çukur, "One model to unite them all: Personalized federated learning of multi-contrast MRI synthesis," *Med Image Anal*, vol. 94, p. 103121, 2024.
- [75] G. Elmas, S. U. Dar, Y. Korkmaz, E. Ceyani, B. Susam, M. Özbey, S. Avestimehr, and T. Çukur, "Federated Learning of Generative Image Priors for MRI Reconstruction," *IEEE Trans Med Imaging*, vol. 42, no. 7, pp. 1996–2009, 2023.
- [76] S. U. Dar, M. Yurt, L. Karacan, A. Erdem, E. Erdem, and T. Çukur, "Image synthesis in multi-contrast MRI with conditional generative adversarial networks," *IEEE Trans. Med. Imag.*, vol. 38, no. 10, pp. 2375–2388, 2019.
- [77] M. Özbey, S. U. Dar, H. A. Bedel, O. Dalmaz, Ş. Öztürk, A. Güngör, and T. Çukur, "Unsupervised medical image translation with adversarial diffusion models," *IEEE Trans Med Imaging*, vol. 42, no. 12, pp. 3524–3539, 2023.
- [78] Z. Yin, K. Xia, S. Wang, Z. He, J. Zhang, and B. Zu, "Unpaired low-dose ct denoising via an improved cycle-consistent adversarial network with attention ensemble," *The Visual Computer*, vol. 39, no. 10, pp. 4423–4444, 2023.
- [79] S. U. H. Dar, M. Özbey, A. B. Çatlı, and T. Çukur, "A transfer-learning approach for accelerated mri using deep neural networks," *Magn. Reson. Med.*, vol. 84, no. 2, pp. 663–685, 2020.
- [80] D. Nie, R. Trullo, J. Lian, L. Wang, C. Petitjean, S. Ruan, and Q. Wang, "Medical image synthesis with deep convolutional adversarial networks," *IEEE Trans. Biomed. Eng.*, vol. 65, no. 12, pp. 2720–2730, 2018.
- [81] M. U. Mirza, O. Dalmaz, H. A. Bedel, G. Elmas, Y. Korkmaz, A. Gungor, S. U. Dar, and T. Çukur, "Learning Fourier-Constrained Diffusion Bridges for MRI Reconstruction," *arXiv:2308.01096*, 2023.
- [82] F. Arslan, B. Kabas, O. Dalmaz, M. Ozbey, and T. Çukur, "Self-consistent recursive diffusion bridge for medical image translation," *arXiv:2405.06789*, 2024.
- [83] D. Nie and D. Shen, "Adversarial Confidence Learning for Medical Image Segmentation and Synthesis," *Int. J. Comput. Vision*, vol. 128, no. 10, pp. 2494–2513, 2020.
- [84] Q. Gao, Z. Li, J. Zhang, Y. Zhang, and H. Shan, "Corediff: Contextual error-modulated generalized diffusion model for low-dose ct denoising and generalization," *IEEE Transactions on Medical Imaging*, 2023.